Photocatalysis-activated SR-AOP over PDINH/MIL-88A(Fe) composites for boosted chloroquine phosphate degradation: Performance, mechanism, pathway and DFT calculations

Xiao-Hong Yi [a], Haodong Ji [b], Chong-Chen Wang [a],*, Yang Li [a], Yu-Hang Li [a], Chen Zhao [a], Ao Wang [a], Huifen Fu [a], Peng Wang [a], Xu Zhao [c], Wen Liu [b],*

[a] Beijing Key Laboratory of Functional Materials for Building Structure and Environment Remediation, School of Environment and Energy Engineering, Beijing University of Civil Engineering and Architecture, Beijing, 100044, PR China
[b] College of Environmental Sciences and Engineering, Peking University, The Key Laboratory of Water and Sediment Sciences, Ministry of Education, Beijing 100871, PR China
[c] Key Laboratory of Drinking Water Science and Technology, Research Center for Eco-Environmental Sciences, Chinese Academy of Sciences, Beijing 100085, PR China

ABSTRACT

PDINH/MIL-88A(Fe) composites (PxMy) were fabricated from MIL-88A(Fe) and perylene-34,910-tetracarboxylic diimide (PDINH) via facile ball-milling strategy. The optimum P25M175 exhibited outstanding degradation performance toward chloroquine phosphate (CQ) by activating peroxydisulfate (PDS) under low power LED visible light. The synergistic effects of photocatalytic activations of PDS via the direct electron transfer PDS activation over P25M175 and indirect electron transfer PDS activation over pristine MIL-88A contributed to the boosted CQ degradation efficiency. The active species capture experimental data and electron spin resonance (ESR) determinations revealed that both active radicals (like $^{\bullet}SO_4^-$, $^{\bullet}OH$, $^{\bullet}O_2^-$, h^+) and nonradical singlet oxygen ($^1O_2$) participated in the CQ decomposition. The CQ degradation pathways and the toxicity evaluation of the intermediates were proposed based on LC–MS determination and DFT calculation. Also, P25M175 demonstrated good reusability and stability. The findings within this work offered deep insights into the mechanisms of organic pollutants degradation via photocatalysis-activated SR-AOP over Fe-MOF photocatalyst.

1. Introduction

Chloroquine phosphate (CQ), with the IUPAC name of N4-(7-Chloro-4-quinolyl)-N1,N1- diethyl-1,4-pentanediamine diphosphate (its chemical structure can be found in Scheme S1), was usually used in the treatment and prevention of malaria as generic pharmaceutical drug [1], the treatment of amebiasis [2] and rheumatoid arthritis [3] as anti-inflammatory agent. In 2020, CQ received increasing attention as a possible treatment for coronavirus disease 2019 (COVID-19) resulted from the severe acute respiratory syndrome coronavirus 2 (SARS-CoV-2) [4].

The persistent and bio-accumulative CQ, as antiviral and antibacterial pharmaceutical, might exert potential threat to living organisms and environment due to its high toxicity. As well, the previous research investigated the transport, transfer and fate of CQ in water environment based on its chemical stability [5]. At these points, it is necessary to

remove the CQ from the contaminated wastewater before being discharged into natural water. In 2020, Bensalah and coworkers adopted electro-Fenton oxidation technology to produce $^{\bullet}OH$ radicals for degrading CQ in simulated wastewater, in which the effects of operating conditions (like pH, current density, oxygen gas flow rate, and anode material), degradation pathway and mechanism were clarified [6]. Recently, sulfate radical-advanced oxidation process (SR-AOP) have attracted increasing attention due to that the $^{\bullet}SO_4^-$ ($E° = 2.5$–3.1 V) radicals demonstrates higher redox potential than $^{\bullet}OH$ ($E° = 1.9$–2.7 V), along with longer half-life time (30–40 μs *versus* 20 ns of $^{\bullet}OH$) and higher selectivity [7]. The $^{\bullet}SO_4^-$ radicals are generally generated from the activation of peroxymonosulfate (PMS, HSO_5^-) and peroxydisulfate (PDS, $S_2O_8^{2-}$) with the aid of light, heat, ultrasound with or without catalysts [8]. Recently, increasing attentions were paid to the field of photocatalysis-activated SR-AOPs with the presence of heterogeneous catalysts upon the irradiation of ultraviolet (UV) light, visible light,

---

UV–vis light or even real solar light [7,9], in which the development of efficient catalysts is of vital importance [10].

Metal-organic frameworks (MOFs) are porous inorganic organic functional materials formed by the coordination and self-assembly of polydentate organic ligands containing O or N atom and transition metal ions [11]. In particular, the abundant nano cavities and open channels in frameworks can provide favorable channels for the entry of the targets to be treated as well as the discharge of the product after treatment, which helps to promote the mass transfer process of catalytic reaction [12]. Besides the above-stated remarkable properties, the well dispersed metal components in MOFs can also provide sufficient active sites for catalytic reaction [13] to achieve high catalytic activity.

Up to now, the individual MOFs, the MOF-based composites and MOF-derivatives were adopted as effective catalysts to activate PMS and PDS for environmental remediation [14]. Especially, Fe-containing MOFs were potential photocatalysis-activated heterogeneous SR-AOPs catalysts due to the presences of both extensive iron-oxo clusters and coordinatively unsaturated Fe sites [15]. The environmentally friendly Fe-MOFs also demonstrated outstanding thermal stability and chemical stability [16]. The abundant coordination unsaturated sites on the surface of Fe-MOFs can also activate persulfate (PS), which can react with photogenerated electrons to inhibit photogenerated electron hole recombination and generate $^\bullet SO_4^-$ to accelerate the degradation of organic pollutants [16]. Some Fe-containing MOFs as emerging photocatalysts can accomplish photocatalytic activation of PS via indirect electron transfer due to the Fe(II)/Fe(III) transformation [7]. However, the individual Fe-containing MOFs photocatalysts suffered from the short lifetimes and fast recombination of photo-induced e^--h^+ pairs. To overcome these drawbacks, some semi-conductors or conductors were introduced to construct photocatalyst composites with Fe-containing MOFs [17,18]. The construction of heterojunctions might promote the separation and migration of photo-induced e^--h^+ pairs to participate in PS activation, resulting into boosted organic pollutants degradation via direct electron transfer [7].

Among various Fe-MOFs, environment friendly MIL-88A(Fe) constructed from Fe^{3+} and fumaric acid was previously used to activate PDS for RhB degradation [19] and TC degradation [16]. Generally, the combination of MOFs and the secondary or even ternary composites like semiconductors, conducting polymers or noble metal atoms can further enhance the photocatalysis activity and stability [18,20]. 34,910-pyrenetetracarboxydiimine (PDINH), as an organic semiconductor photocatalyst, attracts increasing interest due to its low cost, good stability and biocompatibility, suitable band gap, along with high electron affinity and carrier mobility [21–23]. Within this work, MIL-88A(Fe) and PDINH were adopted to fabricate PDINH/MIL-88A composites (P*x*M*y*) via facile ball-milling procedure to construct PDINH/MIL-88A/PDS/visible light system, in which CQ was selected as model contaminant to test the corresponding performance. To the best of our knowledge, it is the first case to construct PDINH/MIL-88A composites by facile ball-milling method, and adopt these composites as photocatalysis-activated SR-AOP catalysts to activate PDS for CQ degradation upon the irradiation of visible light. This work aimed to clarify the following issues: (i) the transfer pathway of the charge carriers between MIL-88A and PDINH; (ii) the formation mechanism of the dominated reactive oxygen species (ROS) in the PDINH/MIL-88A/PDS/visible light system; (iii) the influence of the factors including PDS concentration, initial solution pH and foreign ions on degradation performance; (iv) CQ degradation pathways and the corresponding detoxification assessment in this system.

2. Experimental

All information of the used materials, detailed characterization instruments and techniques, as well as the DFT calculation details are provided in the Supplementary Information (SI).

2.1. Synthesis of PDINH/MIL-88A(Fe) (PxMy) composites

The solvothermal synthesis of spindle-like MIL-88A was carried out according to the method previously reported [17]. The solutions of FeCl$_3$·6H$_2$O (5 mmol, 1.352 *g*) and fumaric acid (5 mmol, 0.580 *g*) dissolved in 50 mL DMF were mixed completely in a 100 mL Teflon-lined, and stirred for 1 h. The MIL-88A(Fe) was produced after the mixture was heated at 100 °C for 12 h, which was separated from the mother solution via centrifugation after cooling to ambient temperature. The as-prepared MIL-88A were further washed twice with DMF and absolute ethanol.

The PDINH/MIL-88A composites were synthesized from the commercially available PDINH and the as-prepared MIL-88A via 4 runs' ball milling (30 Hz, 5 min each run). The obtained PDINH /MIL-88A composites with different mass ratios can be referred as P*x*M*y*, in which the letters "P" and "M" are abbreviated as PDINH and MIL-88A, as well as the variables "*x*" and "*y*" are the mass fraction of PDINH and MIL-88A in the composites, respectively.

2.2. Evaluation photocatalysis-activated SR-AOP performances of PxMy composites

50.0 mL chloroquine phosphate aqueous solution with an initial concentration of 10.0 mg L^{-1} was selected to evaluate the photocatalysis-activated SR-AOP performances over P*x*M*y* composites with a catalyst dosage of 400.0 mg L^{-1} under the irradiation of 300 ± 50 mW LED visible light (PCX50C, Beijing Perfectlight Technology Co., Ltd, the light spectrum was shown in Fig. S1). After the adsorption-desorption equilibrium was accomplished in 1 h under dark condition, a certain amount of persulfate solution was added, then the target solution was irradiated with the LED visible light. During the illumination period, 1.0 mL solution was filtrated from the reactor every 5 min or 10 min for subsequent determination. 10 μL methanol was added to the filtrate to avoid the further reaction between the residual CQ and the ROS before determination. The concentrations of residual CQ in the filtrate was determined by ultra-high performance liquid chromatography (UHPLC, Thermo Scientific Vanquish Flex), which was equipped with a UV–vis detector and a C18 reversed-phase column (2.1 mm × 100 mm, 1.7 μm). The mobile phase consisted of acetonitrile and 0.3 % triethylamine (adjust pH to 3.3 with phosphoric acid) (10/90, *v/v*) with the flow rate of 0.350 mL min^{-1} and a column temperature of 40 °C. The injection volume was 20 μL and the detection wavelength was 342 nm. The concentration of degradation products were determined by UHPLC coupled with LC–MS (UHPLC, Dionex UltiMate 3000 Series; MS, Q Exactive, USA) and the details were appended in Supplementary Information.

3. Results and discussion

3.1. Characterization of PDINH/MIL-88A(Fe) (PxMy) composites

The surface morphology of as-synthesized samples was identified via SEM, TEM and HRTEM. Fig. 1a and d shows that the original MIL-88A displays smooth spindle-like morphology with particle size of ca. 500–1000 nm. The commercially available PDINH demonstrates block-like shape with particle size in the range of 200–500 nm (Fig. 1b and e). The SEM, TEM and HRTEM observations revealed that PDINH particles were wrapped over the surface of MIL-88A spindles in the optimal P25M175, in which the morphology of MIL-88A was maintained well after the ball milling treatment (Fig.1c, f and S2). The successful fabrication of PDINH/MIL-88A composite (P25M175) was affirmed by the uniform distribution of Fe (characteristic element of MIL-88A) and N (characteristic element of PDINH) from the EDS elemental mappings (Fig. 1g).

The PXRD patterns of PDINH, MIL-88A, and series PDINH/MIL-88A (Fe) (P*x*M*y*) composites were shown in Fig. 2a. It should be noted that
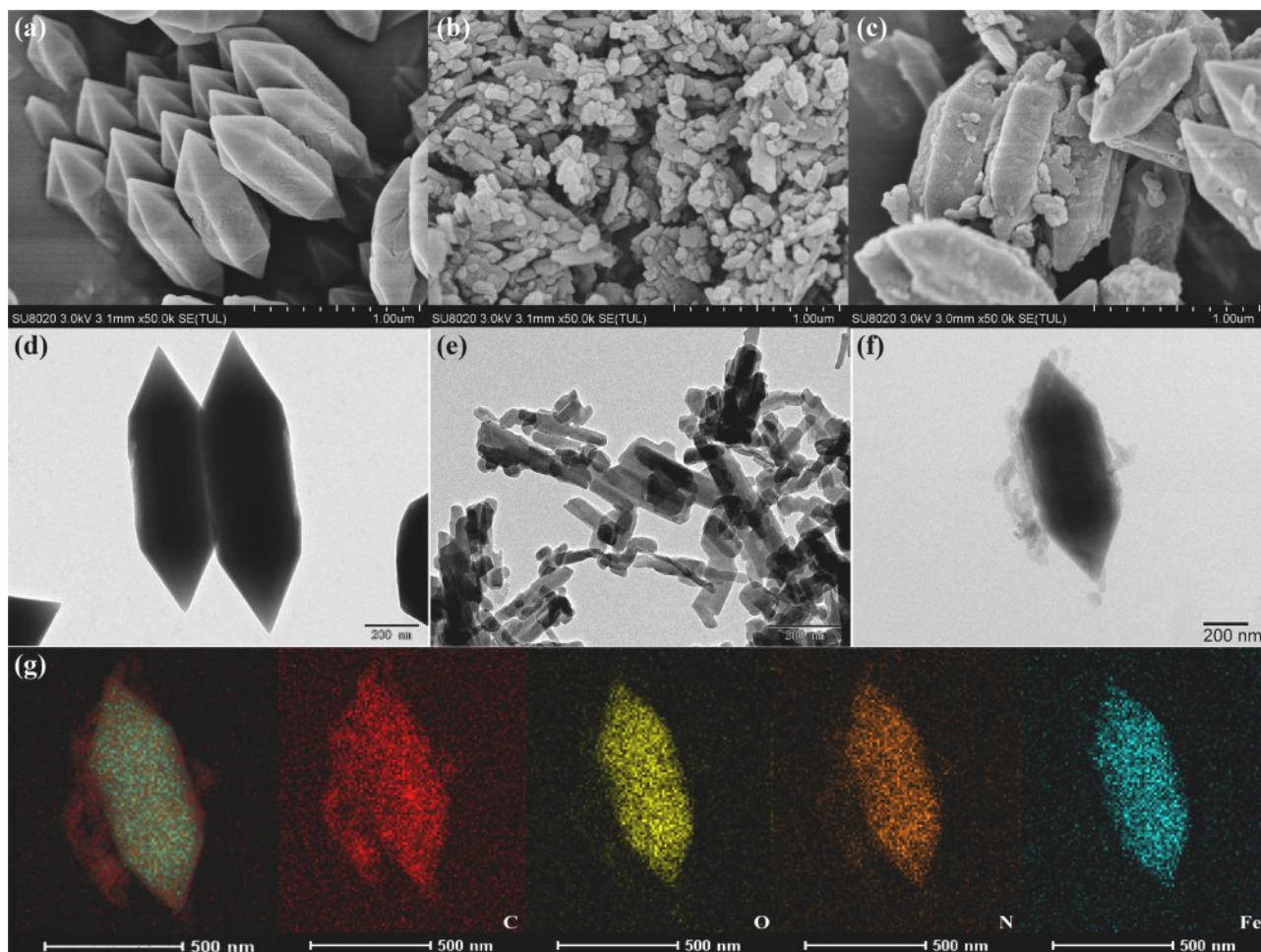
Fig. 1. The SEM and TEM images of (a, d) pristine MIL-88A(Fe), (b, e) pristine PDINH, (c) and (d) P25M175 composite; (g) The EDS elemental mappings of the P25M175 composite.

the positions of all peaks for MIL-88A were well matched with the related references [24]. The three diffraction peaks at $2\theta = 8°$, $10.4°$ and $12.9°$ could be assigned to (100), (101) and (002) facets of MIL-88A respectively [24]. In the PXRD patterns of PDINH/MIL-88A composites, the main peaks could be observed in those of both PDINH and MIL-88A, indicating that PDINH/MIL-88A composites were successfully obtained after ball-milling. In addition, the characteristic peak intensity at $2\theta = 27.04°$ of PDINH gradually rises with the increased PDINH content. The composition of PxMy composites was confirmed by FTIR analysis (Fig. 2b). The typical peaks at ca. 1605.45 cm^{-1} and 1216.97 cm^{-1} were ascribed to the stretching vibration of C=C or C=O and C—O group of Fumarate in MIL-88A [25–27], respectively. The peak located at 1686.35 cm^{-1} could be the asymmetric vibration of C=O in PDINH [28]. The peaks located from 1600 cm^{-1} to 1500 cm^{-1} could be attributed to C—N stretching vibrations and N—H bonding of PDINH [29]. In addition, Fe-O stretching vibration peak (560.7 cm^{-1}) was observed in both MIL-88A(Fe) and PxMy, further confirming the successful combination of MIL-88A(Fe) and PDINH.

To explore the surface element information of PxMy composites, P25M175 was selected as the representative sample to conduct XPS characterization and analysis. As shown in Fig. 2c, P25M175 contains C, O, Fe and N elements, which matches well with the EDS test results. In the Fe 2p XPS spectrum, the two peaks located at ca. 711.4 eV and 725 eV ($\Delta = 13.6$ eV) are related to the Fe 2p$^{3/2}$ and Fe 2p$^{1/2}$ (Fig. 2d), respectively [19,30–32]. The fitting peaks at 716.8 eV and 727.43 eV are usually assigned to the satellite peak of Fe 2p$^{3/2}$ and Fe 2p$^{1/2}$. In all, the four fitting peaks are related to the Fe^{3+}, which prove that the presence

of Fe^{3+} in MIL-88A structure [30,31,33].

The optical features and light absorption ability of MIL-88A(Fe), PDINH and PxMy were characterized through the UV–vis DRS spectra. It was evident that all three catalysts can absorb light in the visible region, indicating that they can be excited by visible light (Fig. 3a). As well, the increasing PDINH content in PxMy composites resulted into similar adsorption behavior of PDINH. The band gaps of MIL-88A(Fe) and PDINH are calculated by Eq. (1) [34]:

$$\alpha(h\nu) = A(h\nu - E_g)^{n/2} \tag{1}$$

where α, h and ν are the absorption coefficient, the light constant, and light frequency, respectively. n is judged by the optical transition type of the semiconductor (indirect ($n = 4$) or direct ($n = 1$)) [35]. Therefore, the band gaps of MIL-88A(Fe) and PDINH were calculated to be 2.75 eV and 1.78 eV, respectively (Fig. 3b). The stronger optical adsorption of PxMy can be improved because of the inherent optical properties of the PDINH. These results indicate that PxMy can be used for photocatalytic reaction under visible light.

3.2. Photocatalysis-activated SR-AOP performances of PxMy composites

3.2.1. CQ degradation

Chloroquine phosphate (CQ) was selected as model pollutant to test the photocatalysis-activated SR-AOP activities of MIL-88A, PDINH and the PxMy composites. The previous research result displayed that, at neutral and acidic conditions, the CQ (pKa = 8.4) was in cationic form [36], while MIL-88A(Fe) and PDINH exhibited positive [31] and
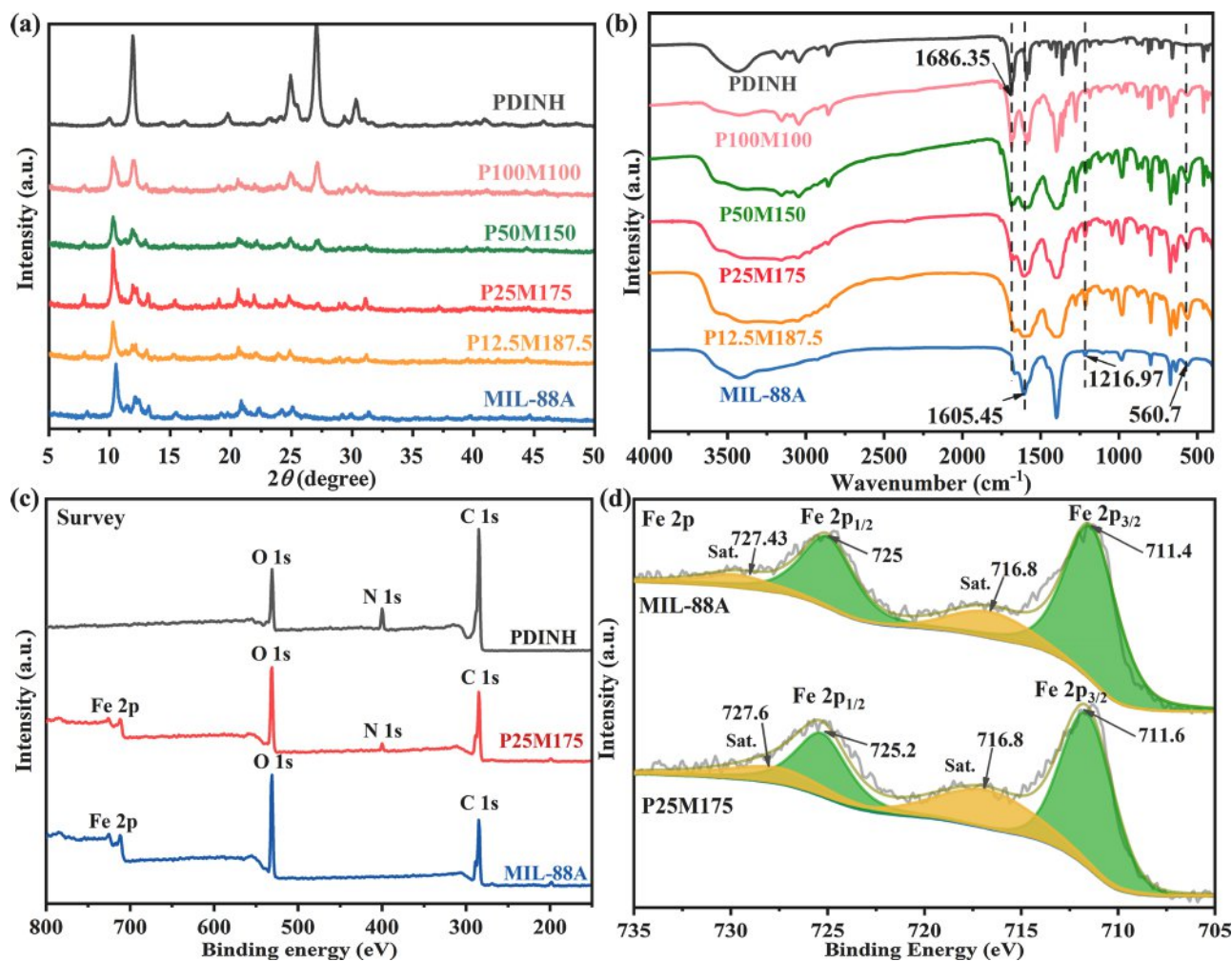
Fig. 2. (a) PXRD and (b) FTIR spectra of as-synthesized materials. (c) Survey and (d) High-resolution XPS spectra of Fe 2p in P25M175 catalyst.
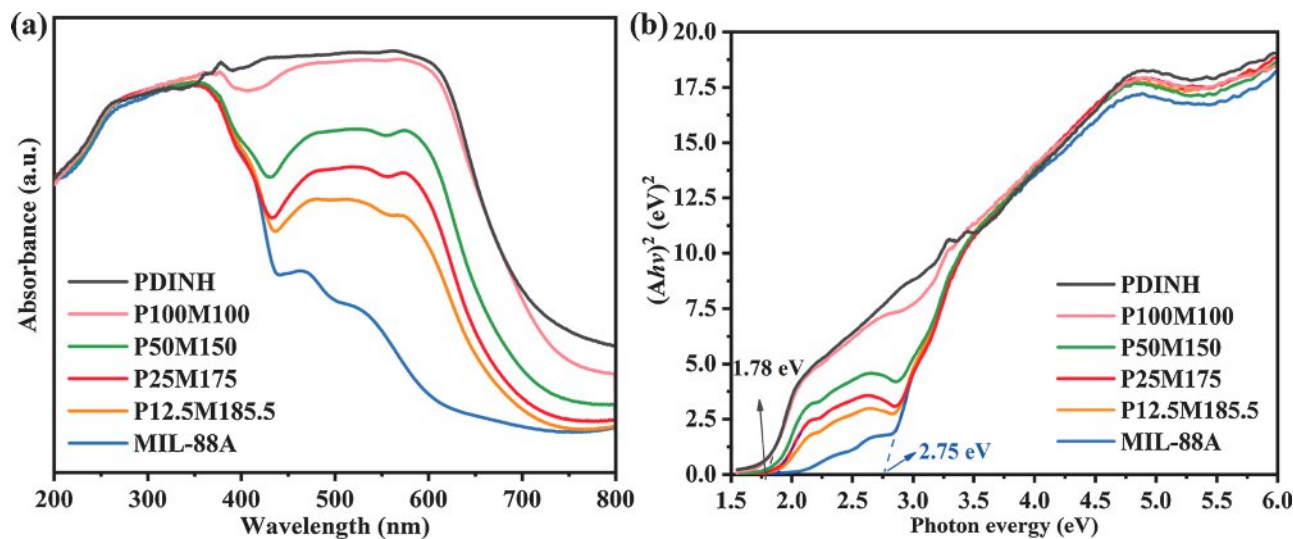

Fig. 3. (a) The UV–vis DRS spectra and (b) the E_g plots of MIL-88A(Fe), PDINH and PxMy composites.

negative zeta potentials [37]. Under dark condition, the pristine MIL-88A exhibited weak adsorption activity toward CQ due to the electrostatic repulsion. While the pure PDINH can accomplish 50 % uptake toward CQ during the adsorption-desorption equilibrium within

1 h because of electrostatic attraction (Fig. 4a). Therefore, it was understandable to find that with the increase of PDINH content in PxMy lead to increasing adsorption ability toward CQ. The SR-AOP degradation performance toward CQ could be boosted by the wrapping PDINH
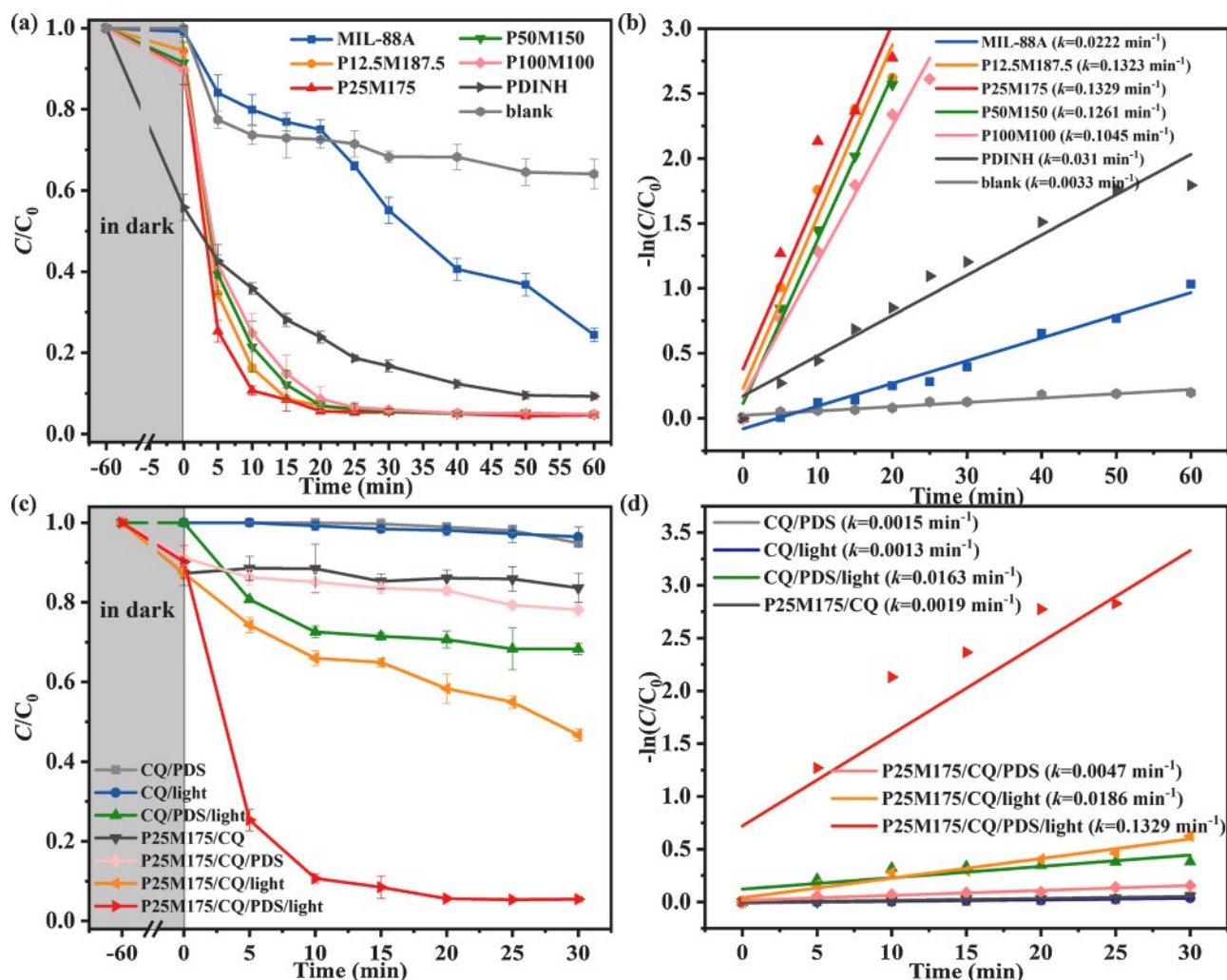
Fig. 4. (a) The photocatalysis-activated SR-AOP CQ degradation efficiencies over different catalysts under visible light. (b) The photocatalysis-activated SR-AOP CQ degradation rates (k values) over different catalysts under visible light. (c) The CQ degradation efficiencies in different systems. (d) The CQ degradation rates (k values) in different systems. Reaction conditions: catalysts $=400$ mg L^{-1}, CQ $=10$ mg L^{-1}, volume $=50$ mL, PDS $=1.0$ mM, pH $= 5.04$.

over the surface of MIL-88A under visible light irradiation. The P25M175 had the best CQ degradation activity, in which the degradation efficiency was 94.6 % within 30 min (Fig. 4a). The reaction kinetics of the CQ degradation over different catalysts were investigated by pseudo-first-order kinetic ($-\ln[C/C_0] = kt$) [20,38]. The results revealed that the apparent reaction rate (k) for the CQ degradation is 0.1329 min^{-1} over P25M175 system, which is 5.99 and 4.29 times as high as those of original MIL-88A(Fe) (0.0222 min^{-1}) and PDINH (0.031 min^{-1}), respectively (Fig. 4b). To affirm the CQ degradation was resulted from photocatalysis-activated SR-AOP process, a series of control experiments were conducted. As illustrated in Fig. 4c, without P25M175 as catalyst, the CQ degradation efficiency can be negligible in the presence of PDS alone (CQ/PDS) or in the presence of light alone (CQ/light). The CQ degradation efficiency increased to 30 % within 30 min in the CQ/PDS/light system. It indicated that some active species could be produced to degrade CQ, once the PDS is excited upon visible light. The CQ oxidation efficiency of P25M175/CQ/light system (53.3 %) was higher than that of P25M175/CQ/PDS system (21.9 %), implying that photocatalysis played an important role in the CQ degradation over P25M175. Notably, the CQ degradation efficiency was dramatically increased to 94.6 % within 30 min in the presence of P25M175, PDS and light, further indicated that more active radicals can be yielded to attack CQ. The role of co-existence of P25M175, PDS and visible light was confirmed by reaction kinetics of the CQ degradation in

different systems fitted by pseudo-first-order kinetic (Fig. 4d).

3.2.2. Effects of PDS dosage and initial solution pH

PDS concentration is known to influence the oxidation process because it is related to the yield efficiency of ROS (like $^{\cdot}SO_4^-$, $^{\cdot}OH$, and $^{\cdot}O_2^-$) and nonradical $^1O_2$ directly. With the increase of PDS concentration from 0.25 mM to 2.0 mM, the CQ removal efficiency increased from 92.6% to 95.7% within 30 min upon the irradiation of visible irradiation (Fig. 5a). The higher PDS concentration could generate more active radicals to enhance the CQ degradation. However, the CQ removal efficiency was maintained at the fixed level when PDS concentration was up to 2 mM. After that, the slightly decreasing CQ degradation efficacy was observed when the PDS concentrations were further increased to 4.0 mM and 8.0 mM. The yield of photo-generated charge carriers is constant over fixed amount of catalyst, which can't satisfy the demand of the excessive PDS as electron acceptors during the reaction procedure (Eqs. (2) and (3)) [17,20,21]. In addition, this also can be explained by the self-quenching reaction between the $^{\cdot}SO_4^-$ and excess PDS as illustrated in Eqs. (4) and (5) [20]. Therefore, PDS with concentration of 2.0 mM was considered to be the optimal dose in the subsequent experiments.
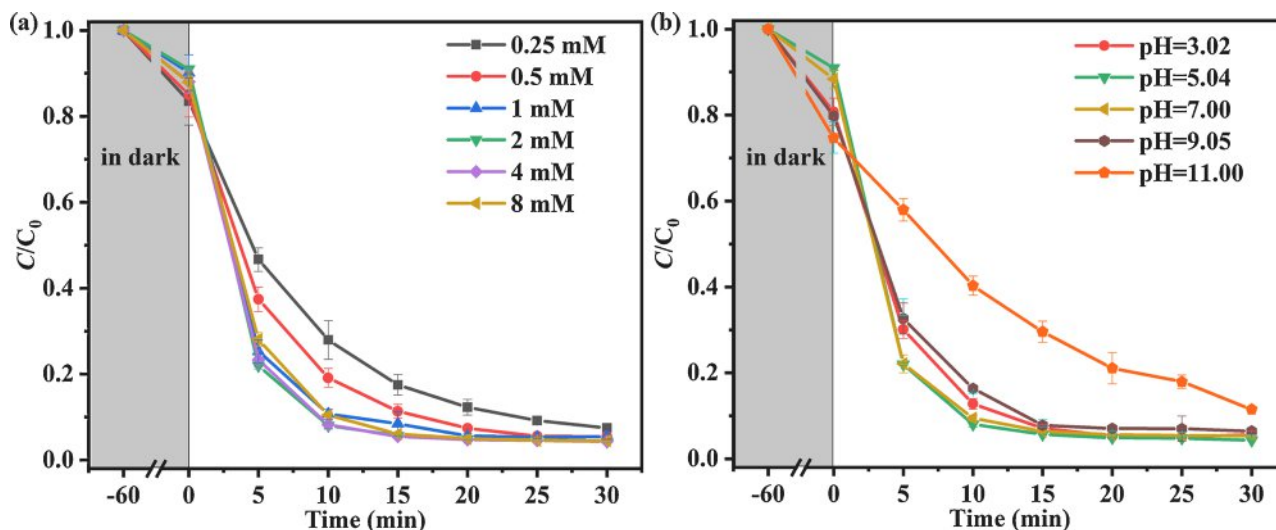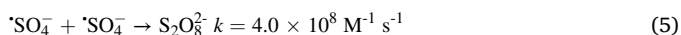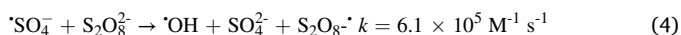
$$P25M175 + light \rightarrow e^- + h^+ \qquad (2)$$

$$S_2O_8^{2-} + e- \rightarrow {^{\cdot}SO_4-} + SO_4^{2-} \qquad (3)$$

Fig. 5. Effects of (a) PDS concentration and (b) initial pH on the CQ degradation over P25M175. Reaction conditions: P25M175 catalysts =400 mg L^{-1}, CQ =10 mg L^{-1}, volume =50 mL, pH = 5.04, PDS =2.0 mM. In the experiments (a) and (b), only one factor was changed, and the other factors were fixed according to the above description.

$$\cdot SO_4^- + S_2O_8^{2-} \rightarrow \cdot OH + SO_4^{2-} + S_2O_8 \cdot^- \quad k = 6.1 \times 10^5 \text{ M}^{-1}\text{ s}^{-1} \quad (4)$$

$$\cdot SO_4^- + \cdot SO_4^- \rightarrow S_2O_8^{2-} \quad k = 4.0 \times 10^8 \text{ M}^{-1}\text{ s}^{-1} \quad (5)$$

The effect of initial pH on the photocatalysis-activated SR-AOP CQ degradation over P25M175 was also investigated. As depicted in Fig. 5b, P25M175 exhibited effective catalytic activity for CQ degradation over a wide initial pH range. It was found that the initial pH of the solution affected the adsorption of CQ on P25M175. Hydrogen-bonding interactions and π-π interaction between the CQ and P25M175 might contribute to its adsorption performance towards CQ (Fig. S3 and Table. S1). With the increase of adsorption at higher pH, the degradation efficiency and rate of CQ decreased. In general, $\cdot SO_4^-$ is more likely to be generated under acidic conditions as listed as Eqs (6) and (7). As well, $\cdot SO_4^-$ can be transformed into SO_4^{2-} and $\cdot OH$ following Eqs. (8) and (9) under alkaline conditions. Considering that $\cdot SO_4^-$ possesses higher oxidation potential ($\cdot SO_4^-$: 2.6–3.1 V *vs.* $\cdot OH$: 1.8-2.7 V) and longer half-life ($\cdot SO_4^-$: 30−40 μs *vs.* $\cdot OH$: 20 ns) than $\cdot OH$ radical [7,39], the photocatalysis-activated SR-AOP reaction rates over P25M175 are faster under acidic conditions than those under alkaline conditions. The corresponding reaction rates are in the order of pH = 5.04 (0.1439 min^{-1}) > pH = 3.02 (0.1377 min^{-1}) > pH = 7.00 (0.1351 min^{-1}) > pH = 9.05 (0.1255 min^{-1}) > pH = 11.00 (0.0615 min^{-1}).

$$S_2O_8^{2-} + H^+ \rightarrow HS_2O_8^- \quad (6)$$

$$HS_2O_8^- + e^- \rightarrow \cdot SO_4^- + SO_4^{2-} + H^+ \quad (7)$$

$$\cdot SO_4^- + H_2O \rightarrow SO_4^{2-} + \cdot OH + H^+ \quad (8)$$

$$\cdot SO_4^- + OH^- \rightarrow \cdot OH + SO_4^{2-} \quad (9)$$

3.2.3. Effects of co-existing ions

The presence of co-existing ions might affect the CQ degradation behaviors during photocatalysis-activated SR-AOP process. The influence of coexisting ions on the photocatalysis-activated SR-AOP process was further investigated by Box-Behnken experimental design methodology [40,41]. It was thought that some inorganic cations (such as K$^+$, Na$^+$, Ca^{2+} and Mg^{2+}) existed in aquatic environment cannot capture e$^-$ or h$^+$ because of the stable and highest oxidation states, which would not show obvious effects on CQ degradation [20,40]. Consequently, just inorganic anions such as Cl$^-$ (A), NO$_3^-$ (B), SO$_4^{2-}$ (C), HCO$_3^-$ (D) and

H$_2$PO$_4^-$ (E) were chosen as experimental variables to investigate the influences toward the CQ degradation efficiencies over P25M175 under LED visible light. The concentration of the five above-stated factors based on the characteristics of surface water quality in some areas of Beijing and subsequent designed experiments (46 runs) were summarized in Table. S2 and S3. At the same time, the results indicated that the response (degradation efficiency %) and independent variables conformed to the quadratic polynomial model as listed in Eq. (10).

Efficiency % = 82.00 + 1.30*A* - 1.38*B* -0.52*C* + 4.85*D* + 2.80*E* - 0.46*AB* - 1.14*AC* + 0.85*AD* - 0.63*AE* + 0.15*BC* + 3.72*BD* + 1.90*BE* - 0.11*CD* + 4.19*CE* - 1.32*DE* - 1.18*A*^{2} - 0.63*B*^{2} - 1.77*C*^{2} - 0.73*D*^{2} - 0.55*E*^{2} (10)

On the basis of the ANOVA results of SR-AOP efficiencies, the R^2 and adjusted R^2 were calculated as 0.9841 and 0.9713, respectively, suggesting that good relationship between the experimental and theoretical values of the response (Table. S4). Besides, the effect of 5 variables on CQ degradation based on the F values of variables fitted the following order: D (764.38) > E (253.85)> A (71.80)> B (61.58)> C (8.84), suggesting that the HCO$_3^-$ has the highest relative importance among the variables, followed by H$_2$PO$_4^-$. The optimum efficiency was fitted by the Box-Behnken methodology with the initial concentrations of Cl$^-$, NO$_3^-$, SO$_4^{2-}$, HCO$_3^-$ and H$_2$PO$_4^-$ were 98.25, 13.60, 100.25, 272.00 and 0.85 mg L^{-1}, respectively (Fig. 6). On the basis of the above experimental and theoretical results, it can be deduced that the photocatalysis-activated SR-AOP degradation efficiency toward CQ over P25M175 decreased with the presence of coexisting inorganic anions. In real situation, the adverse impact of the co-existing ions can be overcome by some strategies like prolonging hydraulic retention time (HRT) or/and increasing the catalyst dosage.

3.3. Possible photocatalysis-activated SR-AOP mechanisms over PxMy composites

To understand the photocatalysis-activated SR-AOP CQ degradation mechanism over P*x*M*y* composites, the band positions of both MIL-88A and PDINH were primarily measured. As shown in Fig. S4a and S4b, the slopes of linear C^{-2} potential curve of MIL-88A and PDINH were positive, indicating that both MIL-88A and PDINH exhibit the properties of n-type semiconductor [17]. The flat band potentials (E_{FB}) of MIL-88A and PDINH were determined as -0.28 eV and -0.4 eV *vs.* Ag/AgCl, respectively. Therefore, the E_{FB} of MIL-88A and PDINH were calculated as -0.08 eV and -0.2 eV *vs.* NHE, respectively. For n-type
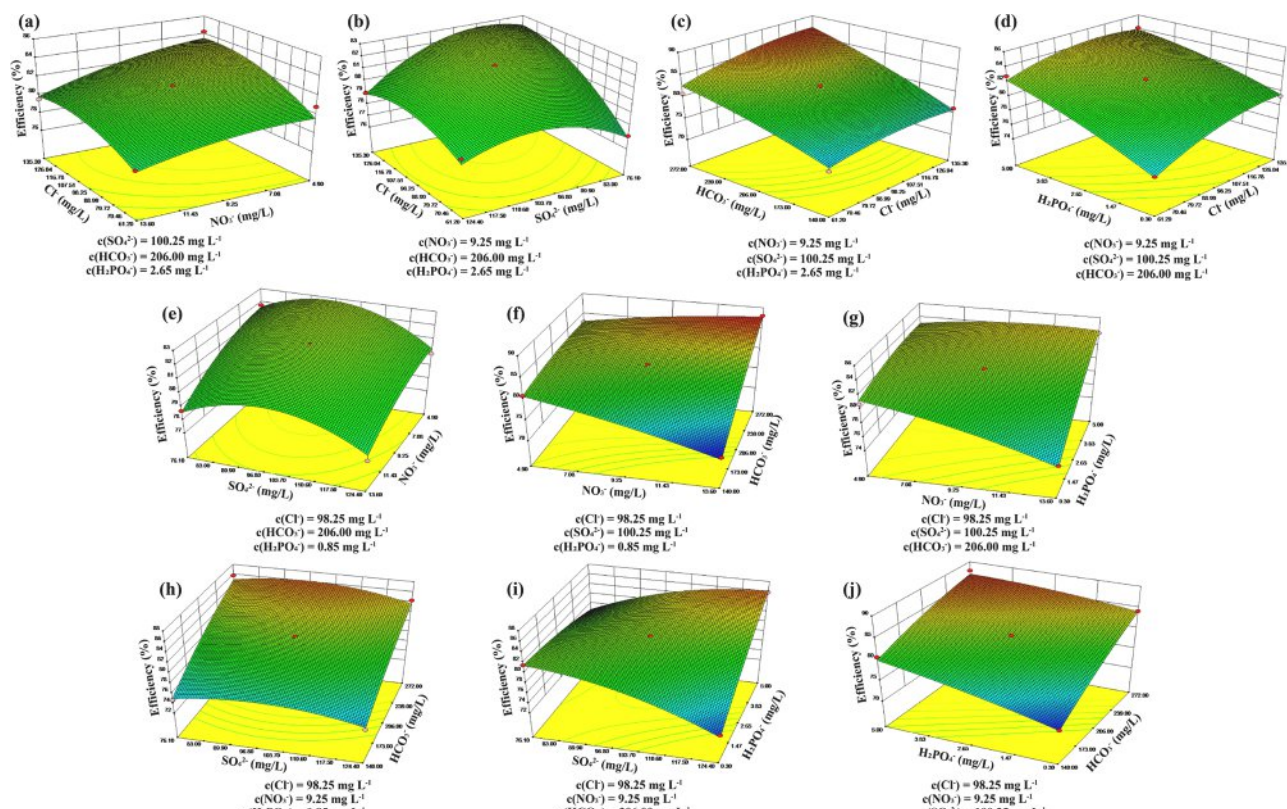
Fig. 6. Response surface graphs of foreign ions (Cl$^-$, NO$_3^-$, SO$_4^{2-}$, HCO$_3^-$ and H$_2$PO$_4^-$) on CQ degradation over P25M175.

semiconductors, the position of E_{FB} is ca. 0.1 eV higher than that of E_{CB} [42]. As well, considering the effect of pH value, the formula ($E = E_0 - 0.05915 \times$ pH) was used to modify the E_{LUMO} of MIL-88A and PDINH [42]. Therefore, the E_{LUMO} of MIL-88A and PDINH were -0.59 eV and -0.71 eV *vs.* NHE at pH = 7.0, which was different from previous studies because of their different synthetic methods [16]. According to the band gap calculated from UV–vis DRS spectrum and the formula of $E_g = E_{VB} - E_{CB}$, the potential of the highest occupied molecular orbital (E_{HOMO}) of MIL-88A and PDINH were 2.16 eV and 1.07 eV *vs.* NHE, respectively.

Based on the above experimental results, the possible photocatalysis-activated SR-AOP degradation mechanism can be proposed as illustrated in Fig. 7. During the catalytic reaction, both MIL-88A and PDINH could produce photogenerated holes and electrons excited by visible light. In view of the perfectly matched band positions of the two components, the photogenerated electrons can migrate from the LUMO orbital of PDINH to the LUMO orbital of MIL-88A for PDS activation to yield ·SO$_4^-$ radicals. Significantly, the redox potential of O$_2$/·O$_2^-$ is -0.33 eV *vs* NHE [20], which is lower than the E_{LUMO} of MIL-88A and PDINH. Therefore, the dissolved oxygen molecules in the reaction system can react with photogenerated electrons to form ·O$_2^-$, which has been proved to be directly involved in the CQ degradation. On the other hand, the photogenerated electrons could be captured by the ·SO$_4^-$ and ·O$_2^-$ effectively, which could accelerate the separation and migration of photogenerated carriers to boost the photocatalysis-activated SR-AOP process.
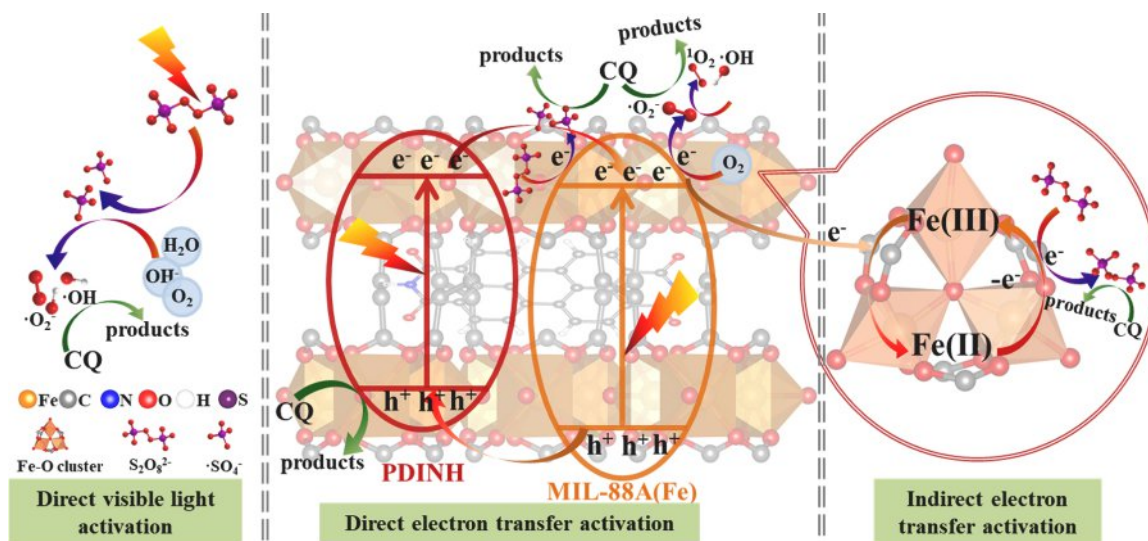

Fig. 7. Illustration of plausible mechanism of photocatalysis-activated SR-AOP oxidation of CQ over P25M175 under LED visible light.

The transportation pathway of charge carries between MIL-88A and PDINH was further studied by DFT calculation. The length and width of PDINH molecule are 14.534 Å and 7.291 Å, and the longest transverse vacancy and longitudinal vacancy are 11.184 Å and 14.591 Å, respectively. Considering that H-bond was easily formed between H and O atoms, the most stable structure can be constructed between PDINH and MIL-88A as illustrated in Fig. S5. And the Bader charge analysis was used to estimate the charge carriers transfer in P25M175 composite. The atoms involved in Bader charge analysis are shown in Fig. 8a. It was found that the charge of PDINH surface atoms decreased by 2.339 eV after combination with MIL-88A(Fe), further affirming that the photo-generated electrons produced in the photo-activation process were transferred from PDINH to MIL-88A(Fe). Generally, Pt^0 nanoparticles (NPs) reduced from H_2PtCl_6 via accepting the electron can be adopted to test the migration path of the photo-generated electron [43]. The photo-deposition of Pt NPs were conducted over P25M175 to further confirm the charge transfer route. The HRTEM images (Fig. 8b and c) showed that the nominal range value of Pt (111) (0.228 nm) was in the same crystal range (0.228 nm) as the characterized Pt nanoparticle, while the lattice spacing is 0.24 nm for smaller particle [44,45]. It can be concluded that the DFT calculation results are consistent with the experimental results, in which the photo-induced electrons migrate from PDINH to MIL-88A in the P25M175 composite.

The active radicals generated in the photocatalysis-activated SR-AOP catalytic reaction was further determined by the active substance capture experiments (Fig. 9a). As previously reported, the reaction rate of methanol capturing ·OH is similar to ·SO_4^- [20]. While the reaction rates of tertbutyl alcohol (TBA) with ·OH (3.8×10^8 M^{-1} S^{-1} to 7.6×10^8 M^{-1} s^{-1}) is faster than that of ·SO_4^- (4.0×10^5 M^{-1} S^{-1} to 9.1×10^5 M^{-1} s^{-1}) [20]. Therefore, TBA was selected to capture ·OH and methanol was adopted to capture both ·OH and ·SO_4^-. It is a remarkable fact that the inhibition influence of methanol on P25M175/light/PDS system is significantly stronger than that of TBA, suggesting that ·SO_4^- is primary active radical for CQ degradation. Also, KI, oxalic acid and L-histidine as scavengers to seize the h^+ on the surface of the catalyst, h^+ in the solution and nonradical singlet oxygen ($^1O_2$) [46]. The CQ degradation efficiency degreased slightly after the addition of TBA, implying the insignificant role of ·OH in SR-AOP reaction. When N_2, KI, oxalic acid and L-histidine were introduced into P25M175/light/PDS system, the catalytic degradation efficiency of CQ decreased significantly, indicating that all ·O_2^-, h^+ and nonradical $^1O_2$ were involved in the SR-AOP degradation toward CQ.

To further determine the active radicals produced in photocatalysis-activated SR-AOP reaction, the radicals produced by MIL-88A, PDINH and P25M175 in dark and visible light irradiation were qualitatively detected by ESR technology. As shown in Fig. 9b, c and d, the results showed that the characteristic intensity of 1:2:2:1 of DMPO-·SO_4^- with PDS and visible light irradiation of MIL-88A, PDINH and P25M175 system, which means that ·SO_4^- was generated in the above systems; there were no DMPO-·OH signal in the dark and visible light irradiation

with MIL-88A, but DMPO-·OH signal was detected after PDS added, which indicates that the ·OH may come from the interaction between ·SO_4^- and H_2O/OH$^-$ [47]. As expected, the composite structure of MIL-88A and PDINH may facilitate the transfer of photogenerated electrons, thus promoting the activation of PDS and producing more significant ·SO_4^- and ·OH signals. At the same time, P25M175/PDS/light can also stimulate the production of other active substances or even nonradical. As shown in Fig. 9c and d, the signals of DMPO-·O_2^- and TEMP-$^1O_2$ were obviously observed in the ESR spectra of P25M175/PDS/light system, and their intensities were relatively stronger than those of P25M175/light system, indicating that the activation of PDS may lead to more·O_2^- and $^1O_2$, thus improving the corresponding SR-AOP performance.

Based on the above analysis results, the catalytic reaction mechanism of this study is shown in Fig. 7. Under visible light irradiation, both MIL-88A and PDINH can produce photogenerated electrons and holes, especially MIL-88A, which can enhance carrier separation and migration efficiency through ligand metal charge transfer process (LMCT) [33]. Due to the good matching of band positions between MIL-88A and PDINH, photogenerated electrons will transfer from the LUMO of PDINH to the LUMO of MIL-88A (-0.59 eV *vs.* NHE). The redox potential position (-0.33 eV *vs.* NHE) of O_2/·O_2^- is more negative than that, so some free photogenerated electrons can react with O_2 to form ·O_2^-, which can directly oxidize and decompose CQ molecules as reactive oxygen species. However, the reason why the degradation rate of CQ increased significantly was that the electron acceptor PDS was added into the reaction system. It can not only capture electrons on the LUMO in MIL-88A and accelerate the separation rate of photogenerated electron hole pairs, but also react with photogenerated electrons to generate ·OH, ·SO_4^- and nonradical $^1O_2$, which can rapidly catalyze the oxidation of CQ molecules. In addition, the Fe_3-μ_3-oxo cluster structure of P25M175 could activate PDS to produce ·SO_4^- through Fenton-like process [20], which can accelerate the oxidative decomposition of CQ. The existence of Fe (II) in XPS analysis of the used P25M175 confirmed the above-stated discussion (Fig. 13d) [48]. Finally, some photogenerated holes can be directly involved in the oxidation of CQ. In conclusion, the catalytic activity of P25M175 composite for the decomposition of CQ is significant with the assistance of PDS and visible light.

The highest efficiency of photocatalysis-activated SR-AOP performance over P25M175 can be explained by the contribution of different pathways of CQ degradation listed as below. (i) The $S_2O_8^{2-}$ is activated by visible light to produce ·SO_4^- in solution, which was also partially transformed into ·OH and ·O_2^-; (ii) The direct electron transfer activation of PDS can produce ·SO_4^- in solution, and some free photogenerated electrons can react with O_2 to form ·O_2^-, $^1O_2$ and ·OH; (iii) The photo-excited electrons facilitates the in situ redox cycles of Fe(II)/Fe(III) in MIL-88A(Fe), which accelerated the PDS activation to yield radicals and improved catalytic performance; (iv) The photo-excited holes can directly participate in CQ degradation, which can simultaneously inhibit the electron-hole recombination.
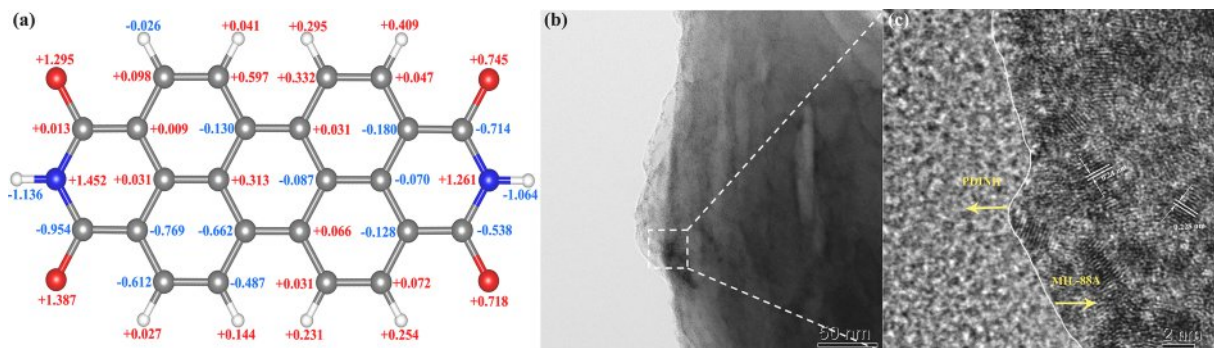

Fig. 8. (a) The Bader charge analysis of PDINH. (b) and (c) HRTEM images of photo-deposited Pt over P25M175.
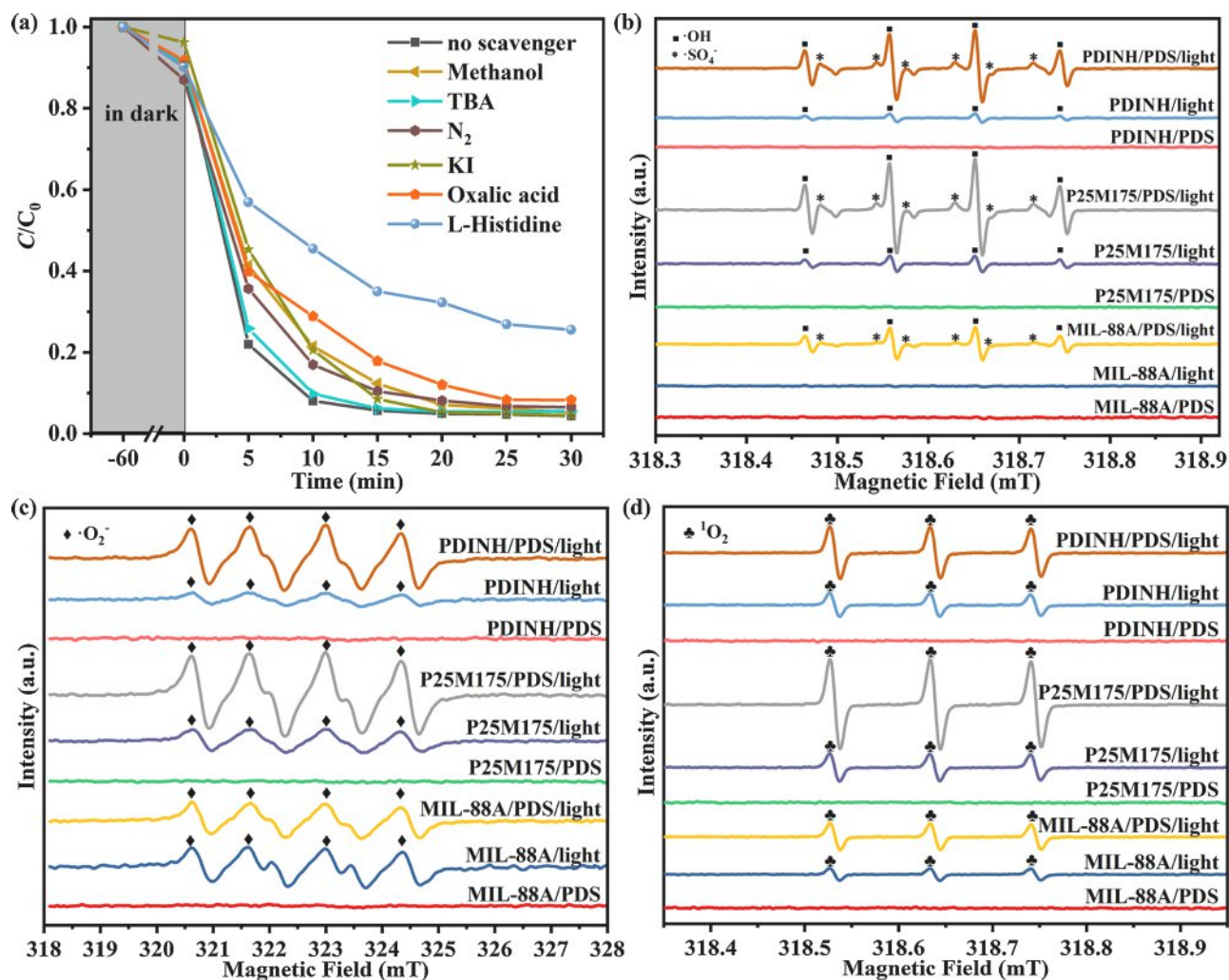
Fig. 9. (a) Effects of different scavengers on CQ degradation in the presence of P25M175. The ESR spectra of (b) DMPO-$^{\cdot}SO_4^-$ and DMPO-$^{\cdot}OH$ (c) DMPO-$^{\cdot}O_2^-$, and (d) TEMP-$^1O_2$ over MIL-88A, PDINH and P25M175.
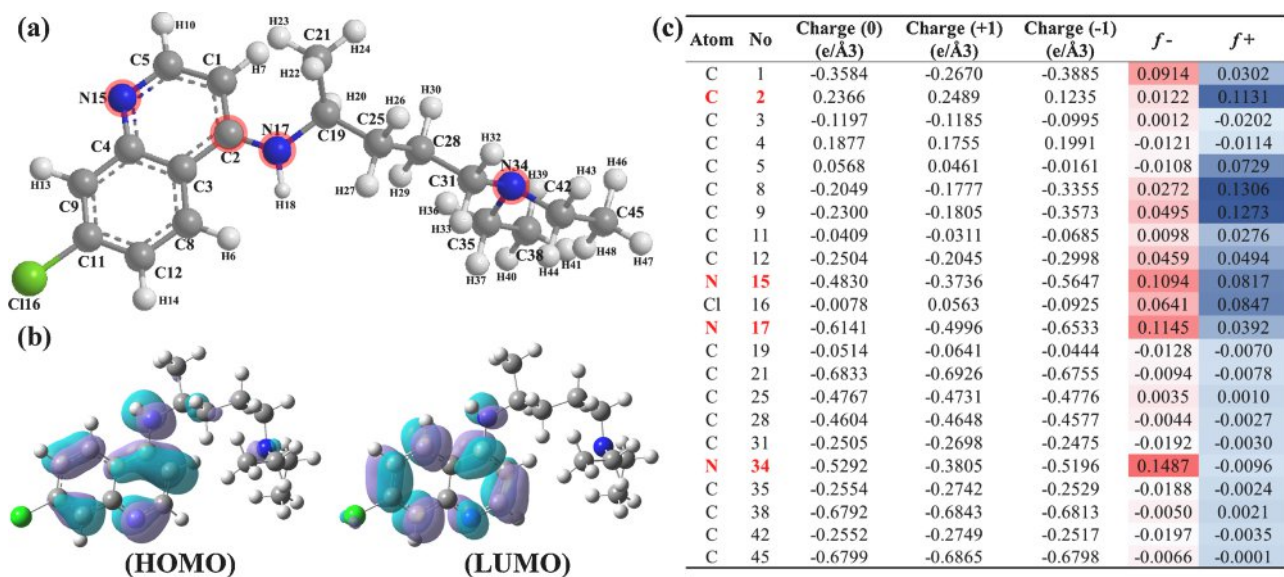

Fig. 10. (a) The Chemical structure, (b) HOMO and LUMO orbitals and (c) Fukui index and NPA charge distribution of CQ.

Atom	No	Charge (0) (e/Å3)	Charge (+1) (e/Å3)	Charge (-1) (e/Å3)	f-	f+
C	1	-0.3584	-0.2670	-0.3885	0.0914	0.0302
C	2	0.2366	0.2489	0.1235	0.0122	0.1131
C	3	-0.1197	-0.1185	-0.0995	0.0012	-0.0202
C	4	0.1877	0.1755	0.1991	-0.0121	-0.0114
C	5	0.0568	0.0461	-0.0161	-0.0108	0.0729
C	8	-0.2049	-0.1777	-0.3355	0.0272	0.1306
C	9	-0.2300	-0.1805	-0.3573	0.0495	0.1273
C	11	-0.0409	-0.0311	-0.0685	0.0098	0.0276
C	12	-0.2504	-0.2045	-0.2998	0.0459	0.0494
N	15	-0.4830	-0.3736	-0.5647	0.1094	0.0817
Cl	16	-0.0078	0.0563	-0.0925	0.0641	0.0847
N	17	-0.6141	-0.4996	-0.6533	0.1145	0.0392
C	19	-0.0514	-0.0641	-0.0444	-0.0128	-0.0070
C	21	-0.6833	-0.6926	-0.6755	-0.0094	-0.0078
C	25	-0.4767	-0.4731	-0.4776	0.0035	0.0010
C	28	-0.4604	-0.4648	-0.4577	-0.0044	-0.0027
C	31	-0.2505	-0.2698	-0.2475	-0.0192	-0.0030
N	34	-0.5292	-0.3805	-0.5196	0.1487	-0.0096
C	35	-0.2554	-0.2742	-0.2529	-0.0188	-0.0024
C	38	-0.6792	-0.6843	-0.6813	-0.0050	0.0021
C	42	-0.2552	-0.2749	-0.2517	-0.0197	-0.0035
C	45	-0.6799	-0.6865	-0.6798	-0.0066	-0.0001

The enhancement effect of photocatalysis-activated SR-AOP over P25M175 was analyzed by electrochemical measurements. The photocurrent response increased significantly while the addition of PDS (Fig. S6a), implying that the PDS addition could weaken the recombination between holes and electrons [18]. Moreover, the Nyquist arc radius of P25M175/light is smaller than P25M175/dark system (Fig. S6b), suggesting that the visible irradiation reduced the charge transfer resistance significantly [49]. What's more, the addition of PDS further reduces the charge transfer resistance of P25M175, indicating that electron transfer is more likely to occur in photocatalysis-activated SR-AOP process.

3.4. CQ degradation pathways and toxicity analysis based on theoretical calculations

DFT calculation was carried out to further elucidate the ROS attack on CQ molecule, which helps to precisely propose CQ degradation pathway in the P25M175/visible light/PDS reaction system. The Fukui index of organic compound was obtained from the PKU-REOD database. Specifically, DFT calculations were conducted to get the Fukui index on nucleophilic (f^+) and electrophilic attack (f^-) according to natural population analysis (NPA) charge distribution of CQ molecule (Fig. 10). Previous studies have widely reported that HOMO and LUMO can describe the sites where organic pollutant molecules are easy to lose or gain electrons in the reaction process [20,50,51]. As shown in Fig. 10b, the purple region and the light blue region represent the electron rich region and the electron poor region of CQ molecule. Therefore, the HOMO mainly locates on the benzene ring and pyridine ring, and thus, the nitrogen atoms in CQ structure are easy to lose electrons, which prefer to be attacked by the electrophilic species like $^\cdot SO_4^-$, $^\cdot OH$, $^\cdot O_2^-$, $^1O_2$ and h^+ [50,52–54]. At the same time, the carbon atoms in CQ structure can be easily attacked by the nucleophilic radicals as they are easy to accept electrons. Fig. 10c presents the Fukui index of different reaction sites of CQ, and the site with higher Fukui index represents greater tendency for radical attack. It is indicated that the N15 ($f^- = 0.1094$), N17 ($f^- = 0.1145$), and N34 ($f^- = 0.1487$) with higher electrophilic attack Fukui values are the most active sites, which are inclined to be attacked by $^\cdot SO_4^-$, $^\cdot OH$, $^\cdot O_2^-$ and $^1O_2$ in this study.

Fig.11 displays the CQ degradation pathway in this system based on UPLC-MS products identification (Fig. S7) and DFT calculation. The degradation of parent CQ ($m/z = 320$) mainly proceeded from the substituents of the side chain, in which there are three primary pathways for CQ degradation: (1) the N34–C35 or N34–C42 cleavage (red line), (2) the N17–C19 cleavage (pink line), and (3) C2–N17 cleavage (green line). The degradation pathway is in good agreement with the DFT calculation results on Fukui index (Fig. 10). Specifically, the oxidative $^\cdot SO_4^-$, $^\cdot OH$, $^\cdot O_2^-$, $^1O_2$ and h^+ would undergo a series of cleavage reactions on the side chain of CQ to form the intermediates like B ($m/z = 292$), C ($m/z = 264$), D ($m/z = 247$), E ($m/z = 159$), F ($m/z = 179$) and G ($m/z = 164$), which was consistent with previous studies [5,6,55–57]. At the same time, the existence of radicals and nonradical species were more likely to attack the side chain of CQ, which was responsible for a series of continuous deamination and ethylation processes. The products H ($m/z = 142$), I ($m/z = 114$), K ($m/z = 102$) and L ($m/z = 159$) were then formed in this process, and the products H and K were further oxidized to obtain the products J ($m/z = 158$) and M ($m/z = 118$). In general, the intermediates could further decompose into low molecular weight compounds like amines and carboxylic acids, which were finally mineralized to H_2O, CO_2, NO_3^-, and NH_4^+ [6,57].

The advantages of an oxidation process can be evaluated by not only decomposition of target pollutants, but also the toxicity of the formed intermediates [49]. The acute toxicity (Fathead minnow and *T. pyriformis*), bioaccumulation factor, developmental toxicity and mutagenicity of CQ and its degradation intermediates were evaluated by using Toxicity Estimation Software (T.E.S.T.) based on quantitative structure-activity relationship (QSAR) prediction [49,50]. The LD_{50} of fathead minnow was 3.07 mg L^{-1} for CQ, which can be categorized as "Toxic" (Fig. 12 a). Nevertheless, the degradation products D and C showed lower LC_{50} value, even the product D was "very toxic". For the further degradation intermediates, the acute toxicity was significantly reduced and the LC_{50} was considered as "Not harmful" for the less toxic products. The 48 h *Tetrahymena pyriformis* IGC_{50} of CQ was 2.14 mg L^{-1}, which was lower than those of degradation products and the several products turned to "Not harmful", suggesting that the growth inhibition of CQ was higher than the degradation products (Fig. 12b). Fig. 12c revealed that the developed photocatalysis-activated SR-AOP process over PxMy system can decrease the bioaccumulation factor of most of the intermediates except product D. In addition, CQ was a "developmental toxicant", while the oxidation process lowered the toxicity of some of degradation products, and products B, C, E, J, K, L, M and Q were even considered as "developmental non-toxicant" (Fig. 12d). Fig. 12e demonstrated that oxidation reaction can reduce the
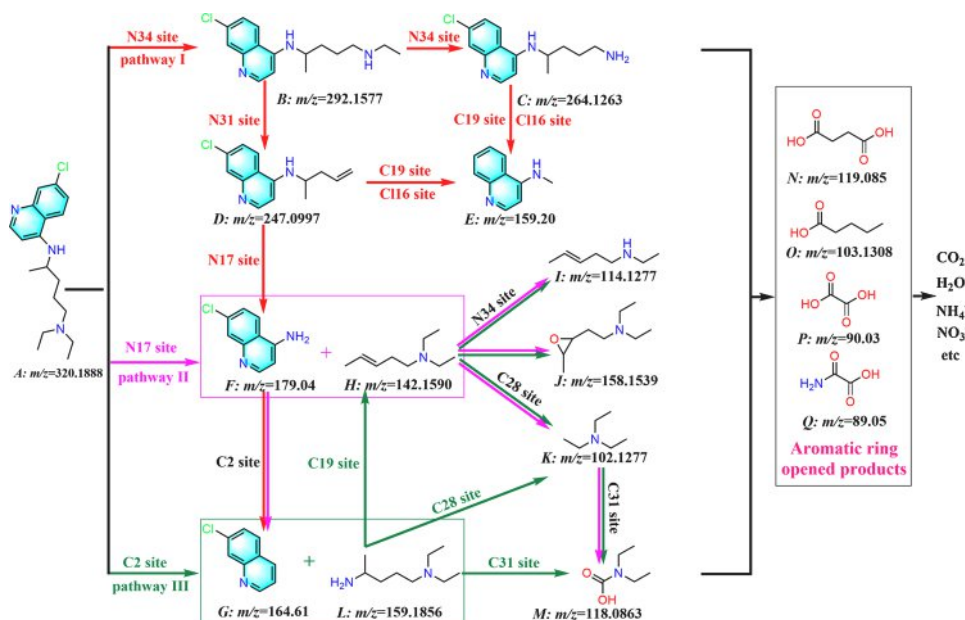

Fig. 11. Proposed CQ degradation pathways by photocatalysis-activated SR-AOP process over P25M175.
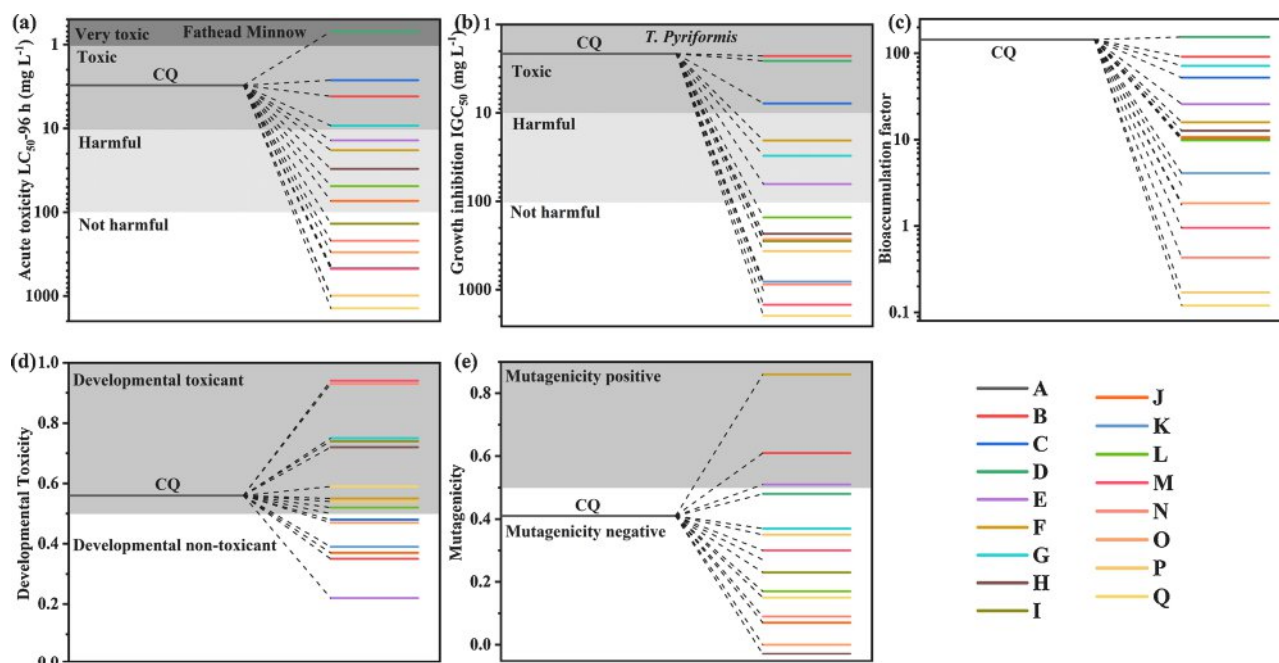
Fig. 12. (a) Fathead minnow LC$_{50}$ (96 h), (b) *T. pyriformis* IGC$_{50}$ (48 h), (c) Bioaccumulation factor, (d) Developmental toxicity and (e) Mutagenicity of CQ and its degradation intermediates.
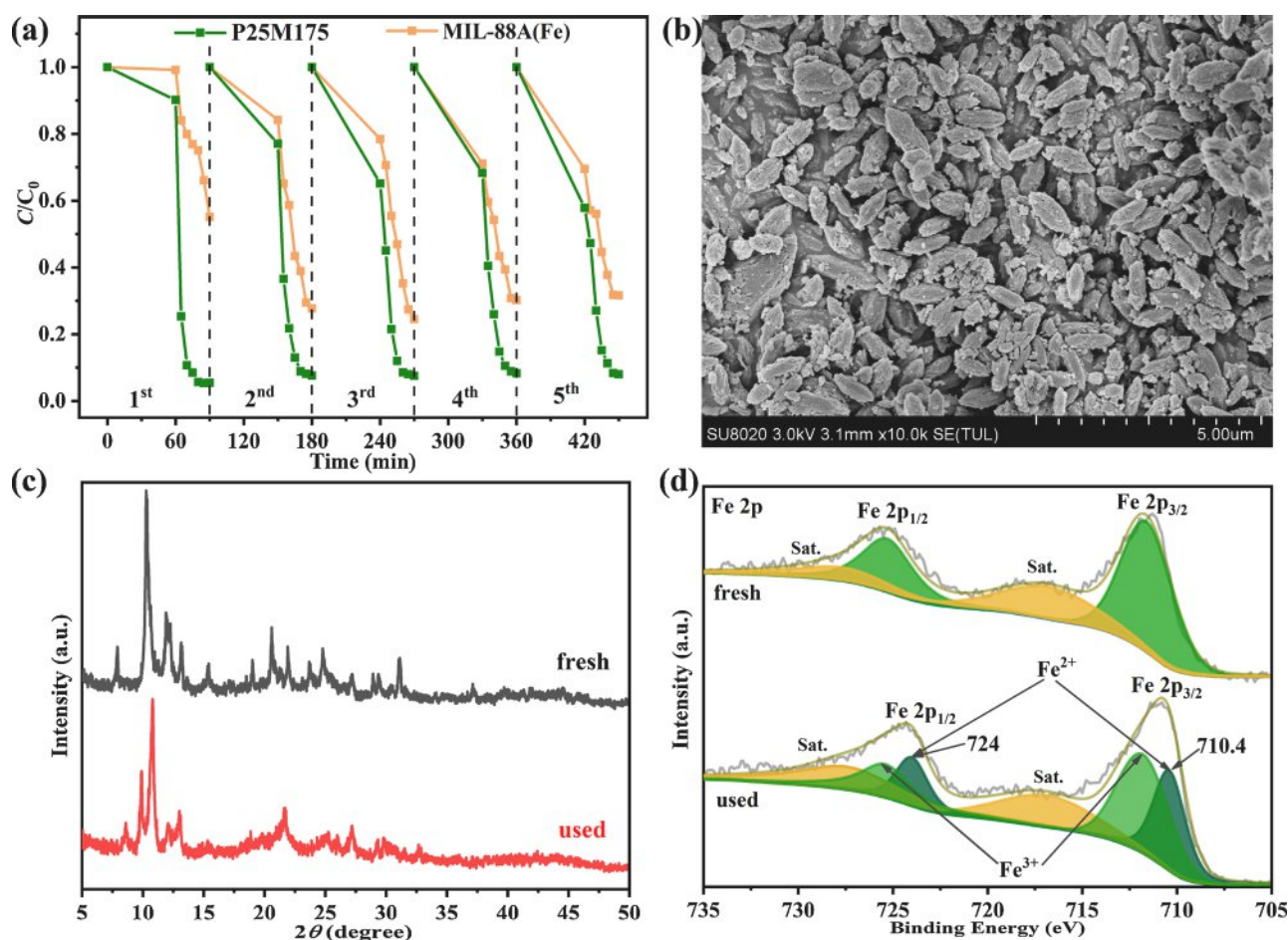

Fig. 13. (a) Photocatalysis-activated SR-AOP degradation of CQ over P25M175 and MIL-88A in five consecutive runs under LED visible light. (b) SEM, (c) PXRD and (d) XPS of P25M175 after photocatalytic degradation of CQ.

mutagenicity of CQ by photocatalysis-activated SR-AOP system. Comprehensive results showed that photocatalysis-activated SR-AOP process over P*x*M*y* system could not only complete removal of CQ but also decrease the toxicity of CQ. COD data were acquired to investigate the CQ mineralization in the photocatalysis-activated SR-AOP process over P25M175. The results revealed that the COD removal efficiency was 38.5 % within 4 h. The extended reaction time or coupled biotechnology were proposed in the future work to accomplish complete mineralization.

3.5. Reusability of P25M175 for the degradation of CQ

To investigate the catalytic stability and recycling of P25M175, five reuse cycles of catalytic experiments were explored in this work. The pristine MIL-88A showed inferior degradation activity, in which 44.9 % and 68.4 % CQ could be removed respectively at the 1 st and 5th cycle under the identical conditions to that of P25M175 (Fig. 13a). However, the degradation efficiency of P25M175 remained about 93.8 % after five reuse cycles of experiments. It is worth noting that CQ will be adsorbed on the surface or pore structure of P25M175, resulting in the decrease of the exposed active sites of P25M175, thus weakening its degradation reaction efficiency. And the above conjecture was confirmed in SEM-Mapping of used P25M175 that displayed the characteristic elements Cl and P of CQ on the used P25M175 (Fig. S8). By comparing the SEM image and PXRD patterns of P25M175 before and after SR-AOP reaction (Fig. 13b and c), it was found that P25M175 still maintained its original morphology and structure after five runs of catalytic experiments, indicating that the good stability and reusability of P25M175. In addition, the concentrations of leached-out Fe were measured using an ICP-OES to further evaluate the stability of MIL-88A and P25M175. The concentrations of leached Fe in the solution were determined by ICP-OES as 1.03 mg L^{-1} and 0.39 mg L^{-1} for individual MIL-88A and P25M175, respectively. Obviously, the introduction of PDINH into P25M175 can significantly reduce Fe leaching and enhance its water stability.

4. Conclusion

The PDINH/MIL-88A (P*x*M*y*) composites were successfully prepared by facile ball-milling, considering the good matching between the band positions of MIL-88A and PDINH. Compared with individual MIL-88A and PDINH, P*x*M*y* composites exhibited superior SR-AOP activity for PDS activation under visible light irradiation, in which the P25M175 could remove ca. 95.7 % of CQ within 30 min under the optimal conditions with 5.99 and 4.29 times higher CQ degradation rate than those of MIL-88A and PDINH, respectively. The enhanced catalytic degradation ability of P25M175 was mainly attributed to the synergistic effects from the different active species (like $^{\bullet}SO_4^-$, $^{\bullet}OH$, $^{\bullet}O_2^-$ and h^+) and non-radical $^1O_2$ yielded via direct visible light activation of PDS, direct electron transfer activation of PDS over P25M175, indirect electron transfer activation of over MIL-88A(Fe). The corresponding migration route of the photoinduced electrons and holes between PDINH and MIL-88A(Fe) in P25M175 was proposed and affirmed by DFT calculations and various experiments tests. It was found that the coexisting anions might exert negative effect on the SR-AOP degradation performance toward CQ, which can be overcome by prolonging hydraulic retention time (HRT) or/and increasing the catalyst input. The CQ degradation pathway was elucidated by LC/MS determination and DFT calculation, and the toxicological simulation revealed that the possible intermediates formed during the CQ degradation exhibited lower toxicity than the pristine CQ. This work provides a new feasible way to remove emerging organic pollutants like CQ via photocatalysis-activated SR-AOP over heterogeneous MIL-88A-based composite catalyst. In our future work, some efforts should be put to accomplish large-scale applications of Fe-MOFs based materials in the real environmental remediation.

CRediT authorship contribution statement

Xiao-Hong Yi: Data curation, Investigation, Visualization, Software, Writing - Original draft preparation, Funding acquisition. **Haodong Ji:** Software, Methodology. **Chong-Chen Wang**: Conceptualization, Funding acquisition, Supervision, Project administration, Writing - review & editing. **Yang Li**: Software, Methodology. **Yu-Hang Li**: Data curation, Software. **Chen Zhao**: Software, Methodology. **Ao Wang**: Instrumental, Drawing. **Huifen Fu**: Methodology, Validation, Software. **Peng Wang**: Resources, Instrumental. **Xu Zhao**: Validation, Writing - review & editing. **Wen Liu**: Validation, Writing - review & editing.

Declaration of Competing Interest

The authors declare no conflict of interest.

Acknowledgements

Appendix A. Supplementary data

Supplementary material related to this article can be found, in the online version, at doi:https://doi.org/10.1016/j.apcatb.2021.120229.

References

[1] J. Rengelshausen, J. Burhenne, M. Fröhlich, Y. Tayrouz, S.K. Singh, K.-D. Riedel, O. Müller, T. Hoppe-Tichy, W.E. Haefeli, G. Mikus, Pharmacokinetic interaction of chloroquine and methylene blue combination against malaria, Eur. J. Clin. Pharmacol. 60 (2004) 709–715, https://doi.org/10.1007/s00228-004-0818-0.

[2] C.W. Hart, R.F. Naunton, The ototoxicity of chloroquine phosphate, Arch. Otolaryngol. 80 (1964) 407–412, https://doi.org/10.1001/archotol.1964.00750040419009.

[3] A. Elman, R. Gullberg, E. Nilsson, I. Rendahl, L. Wachtmeister, Chloroquine retinopathy in patients with rheumatoid arthritis, Scand. J. Rheumatol. 5 (1976) 161–166, https://doi.org/10.3109/03009747609165456.

[4] M. Huang, M. Li, F. Xiao, P. Pang, J. Liang, T. Tang, S. Liu, B. Chen, J. Shu, Y. You, Preliminary evidence from a multicenter prospective observational study of the safety and efficacy of chloroquine for the treatment of COVID-19, Sci. Rev. 7 (2020) 1428–1436, https://doi.org/10.1093/nsr/nwaa113.

[5] A.S. Coelho, C.E.P. Chagas, R.M. de Pádua, G.A. Pianetti, C. Fernandes, A comprehensive stability-indicating HPLC method for determination of chloroquine in active pharmaceutical ingredient and tablets: identification of oxidation impurities, J. Pharm. Biomed. Anal. 145 (2017) 248–254, https://doi.org/10.1016/j.jpba.2017.06.023.

[6] S. Midassi, A. Bedoui, N. Bensalah, Efficient degradation of chloroquine drug by electro-Fenton oxidation: effects of operating conditions and degradation mechanism, Chemosphere 260 (2020) 127558, https://doi.org/10.1016/j.chemosphere.2020.127558.

[7] J. Yang, M. Zhu, D.D. Dionysiou, What is the role of light in persulfate-based advanced oxidation for water treatment? Water Res. 189 (2021) 116627, https://doi.org/10.1016/j.watres.2020.116627.

[8] J. Lee, U. von Gunten, J.-H. Kim, Persulfate-based advanced oxidation: critical assessment of opportunities and roadblocks, Environ. Sci. Technol. 54 (2020) 3064–3081, https://doi.org/10.1021/acs.est.9b07082.

[9] G. Chen, Y. Yu, L. Liang, X. Duan, R. Li, X. Lu, B. Yan, N. Li, S. Wang, Remediation of antibiotic wastewater by coupled photocatalytic and persulfate oxidation system: a critical review, J. Hazard. Mater. (2020) 124461, https://doi.org/10.1016/j.jhazmat.2020.124461.

[10] J. Yu, Z. Zhu, H. Zhang, X. Shen, Y. Qiu, D. Yin, S. Wang, Persistent free radicals on N-doped hydrochar for degradation of endocrine disrupting compounds, Chem. Eng. J. 398 (2020) 125538, https://doi.org/10.1016/j.cej.2020.125538.

[11] X.-Y. Xu, C. Chu, H. Fu, X.-D. Du, P. Wang, W. Zheng, C.-C. Wang, Light-responsive UiO-66-NH$_2$/Ag$_3$PO$_4$ MOF-nanoparticle composites for the capture and release of sulfamethoxazole, Chem. Eng. J. 350 (2018) 436–444, https://doi.org/10.1016/j.cej.2018.06.005.

[12] C.-C. Wang, X. Wang, W. Liu, The synthesis strategies and photocatalytic performances of TiO$_2$/MOFs composites: a state-of-the-art review, Chem. Eng. J. 391 (2020) 123601, https://doi.org/10.1016/j.cej.2019.123601.

[13] C. Gao, S. Chen, X. Quan, H. Yu, Y. Zhang, Enhanced Fenton-like catalysis by iron-based metal organic frameworks for degradation of organic pollutants, J. Catal. 356 (2017) 125–132, https://doi.org/10.1016/j.jcat.2017.09.015.

[14] Z. Xiong, Y. Jiang, Z. Wu, G. Yao, B. Lai, Synthesis strategies and emerging mechanisms of metal-organic frameworks for sulfate radical-based advanced oxidation process: a review, Chem. Eng. J. (2020) 127863, https://doi.org/10.1016/j.cej.2020.127863.

[15] X. Yi, C. Wang, Elimination of emerging organic contaminants in wastewater by advanced oxidation process over iron-based MOFs and their composites, Prog. Chem. (2020), https://doi.org/10.7536/PC200562.

[16] Y. Zhang, J. Zhou, X. Chen, L. Wang, W. Cai, Coupling of heterogeneous advanced oxidation processes and photocatalysis in efficient degradation of tetracycline hydrochloride by Fe-based MOFs: synergistic effect and degradation pathway, Chem. Eng. J. 369 (2019) 745–757, https://doi.org/10.1016/j.cej.2019.03.108.

[17] D.-D. Chen, X.-H. Yi, L. Ling, C.-C. Wang, P. Wang, Photocatalytic Cr(VI) sequestration and photo-Fenton bisphenol A decomposition over white light responsive PANI/MIL-88A(Fe), Appl. Organomet. Chemi. 34 (2020) e5795, https://doi.org/10.1002/aoc.5795.

[18] J.-W. Wang, F.-G. Qiu, P. Wang, C. Ge, C.-C. Wang, Boosted bisphenol A and Cr(VI) cleanup over Z-scheme WO$_3$/MIL-100 (Fe) composites under visible light, J. Clean. Prod. 279 (2020) 123408, https://doi.org/10.1016/j.jclepro.2020.123408.

[19] K.-Y.A. Lin, H.-A. Chang, C.-J. Hsu, Iron-based metal organic framework, MIL-88A, as a heterogeneous persulfate catalyst for decolorization of Rhodamine B in water, RSC Adv. 5 (2015) 32520–32530, https://doi.org/10.1039/C5RA01447F.

[20] C. Zhao, J. Wang, X. Chen, Z. Wang, H. Ji, L. Chen, W. Liu, C.-C. Wang, Bifunctional Bi$_{12}$O$_{17}$Cl$_2$/MIL-100(Fe) composites toward photocatalytic Cr(VI) sequestration and activation of persulfate for bisphenol A degradation, Sci. Total Environ. 752 (2021) 141901, https://doi.org/10.1016/j.scitotenv.2020.141901.

[21] K. Zhang, J. Wang, W. Jiang, W. Yao, H. Yang, Y. Zhu, Self-assembled perylene diimide based supramolecular heterojunction with Bi$_2$WO$_6$ for efficient visible-light-driven photocatalysis, Appl. Catal. B: Environ. 232 (2018) 175–181, https://doi.org/10.1016/j.apcatb.2018.03.059.

[22] Y. Sheng, H. Miao, J. Jing, W. Yao, Y. Zhu, Perylene diimide anchored graphene 3D structure via π-π interaction for enhanced photoelectrochemical degradation performances, Appl. Catal. B: Environ. 272 (2020) 118897, https://doi.org/10.1016/j.apcatb.2020.118897.

[23] Q. Ji, X. Cheng, Y. Wu, W. Xiang, H. He, Z. Xu, C. Xu, C. Qi, S. Li, L. Zhang, S. Yang, Visible light absorption by perylene diimide for synergistic persulfate activation towards efficient photodegradation of bisphenol A, Appl. Catal. B: Environ. 282 (2021) 119579, https://doi.org/10.1016/j.apcatb.2020.119579.

[24] V.P. Viswanathan, S.V. Mathew, D.P. Dubal, N.N. Adarsh, S. Mathew, Exploring the effect of morphologies of Fe(III) metal-organic framework MIL-88A(Fe) on the photocatalytic degradation of rhodamine B, ChemistrySelect 5 (2020) 7534–7542, https://doi.org/10.1002/slct.202001670.

[25] T.S. Alomar, N. AlMasoud, M.A. Awad, M.F. El-Tohamy, D.A. Soliman, An eco-friendly plant-mediated synthesis of silver nanoparticles: characterization, pharmaceutical and biomedical applications, Mater. Chem. Phys. 249 (2020) 123007, https://doi.org/10.1016/j.matchemphys.2020.123007.

[26] G.A. El-Chaghaby, Y.M. Abd El-Shafea, Kinetics and equilibrium of phosphate adsorption onto chemically activated carbon prepared from date stones, Int. J. Dev. Sustain. 6 (2021) 427–438.

[27] S.M. Arde, G.S. Rashinkar, S.N. Jadhav, A.D. Patil, R.S. Salunkhe, Biogenic synthesis of palladium nanoparticles using Boswellia sarrata and their applications in cross-coupling reactions, Appl. Organomet. Chemi. 34 (2020) e6012, https://doi.org/10.1002/aoc.6012.

[28] A. Sahana, A. Banerjee, S. Lohar, B. Sarkar, S.K. Mukhopadhyay, D. Das, Rhodamine-based fluorescent probe for Al^{3+} through time-dependent PET–CHEF–FRET processes and its cell staining application, Inorg. Chem. 52 (2013) 3627–3633, https://doi.org/10.1021/ic3019953.

[29] M.K. Grewal, T. Huppertz, T. Vasiljevic, FTIR fingerprinting of structural changes of milk proteins induced by heat treatment, deamidation and dephosphorylation, Food Hydrocoll. 80 (2018) 160–167, https://doi.org/10.1016/j.foodhyd.2018.02.010.

[30] Q. Chen, J. Li, L. Cheng, H. Liu, Construction of CdLa$_2$S$_4$/MIL-88A(Fe) heterojunctions for enhanced photocatalytic H$_2$-evolution activity via a direct Z-scheme electron transfer, Chem. Eng. J. 379 (2020) 122389, https://doi.org/10.1016/j.cej.2019.122389.

[31] D. Pang, C.-C. Wang, P. Wang, W. Liu, H. Fu, C. Zhao, Superior removal of inorganic and organic arsenic pollutants from water with MIL-88A (Fe) decorated on cotton fibers, Chemosphere 254 (2020) 126829, https://doi.org/10.1016/j.chemosphere.2020.126829.

[32] G. Ren, K. Zhao, L. Zhao, A Fenton-like method using ZnO doped MIL-88A for degradation of methylene blue dyes, RSC Adv. 10 (2020) 39973–39980, https://doi.org/10.1039/D0RA08076D.

[33] N. Liu, W. Huang, X. Zhang, L. Tang, L. Wang, Y. Wang, M. Wu, Ultrathin graphene oxide encapsulated in uniform MIL-88A(Fe) for enhanced visible light-driven photodegradation of RhB, Appl. Catal. B: Environ. 221 (2018) 119–128, https://doi.org/10.1016/j.apcatb.2017.09.020.

[34] H. Jia, W. He, B. Zhang, L. Yao, X. Yang, Z. Zheng, Facile synthesis of bismuth oxyhalide nanosheet films with distinct conduction type and photo-induced charge carrier behavior, Appl. Surf. Sci. 441 (2018) 832–840, https://doi.org/10.1016/j.apsusc.2018.02.030.

[35] X.-H. Yi, S.-Q. Ma, X.-D. Du, C. Zhao, H. Fu, P. Wang, C.-C. Wang, The facile fabrication of 2D/3D Z-scheme g-C$_3$N$_4$/UiO-66 heterojunction with enhanced photocatalytic Cr(VI) reduction performance under white light, Chem. Eng. J. 375 (2019) 121944, https://doi.org/10.1016/j.cej.2019.121944.

[36] E.I. Karim, K. Ibrahim, A. Abdelrahman, A. Fell, Photodegradation studies on chloroquine phosphate by high-performance liquid chromatography, J. Pharm. Biomed. Anal. 12 (1994) 667–674, https://doi.org/10.1016/0731-7085(93)E0026-J.

[37] D. Liu, J. Wang, X. Bai, R. Zong, Y. Zhu, Self-assembled PDINH supramolecular system for photocatalysis under visible light, Adv. Mater. 28 (2016) 7284–7290, https://doi.org/10.1002/adma.201601168.

[38] C. Cui, M. Zhang, X. Yao, S. Tu, Z. Hou, V.S.J. En, X. Xiang, J. Lin, T. Cai, N. Shen, Dose selection of chloroquine phosphate for treatment of COVID-19 based on a physiologically based pharmacokinetic model, Acta Pharm. Sin. B 10 (2020) 1216–1227, https://doi.org/10.1016/j.apsb.2020.04.007.

[39] P. Hu, M. Long, Cobalt-catalyzed sulfate radical-based advanced oxidation: a review on heterogeneous catalysts and applications, Appl. Catal. B: Environ. 181 (2016) 103–117, https://doi.org/10.1016/j.apcatb.2015.07.024.

[40] Y.-X. Li, X. Wang, C.-C. Wang, H. Fu, Y. Liu, P. Wang, C. Zhao, S-TiO$_2$/UiO-66-NH$_2$ composite for boosted photocatalytic Cr(VI) reduction and bisphenol A degradation under LED visible light, J. Hazard. Mater. 399 (2020) 123085, https://doi.org/10.1016/j.jhazmat.2020.123085.

[41] C. Zhao, Z. Wang, X. Li, Y. Yi, H. Chu, X. Chen, C.-C. Wang, Facile fabrication of BUC-21/Bi$_{24}$O$_{31}$Br$_{10}$ composites for enhanced photocatalytic Cr(VI) reduction under white light, Chem. Eng. J. 389 (2020) 123431, https://doi.org/10.1016/j.cej.2019.123431.

[42] J. Liu, X. Zhang, Q. Zhong, J. Li, H. Wu, B. Zhang, L. Jin, H.B. Tao, B. Liu, Electrostatic self-assembly of a AgI/Bi$_2$Ga$_4$O$_9$ p–n junction photocatalyst for boosting superoxide radical generation, J. Mate. Chem. A 8 (2020) 4083–4090, https://doi.org/10.1039/C9TA13724F.

[43] X. Liu, H. Zhai, P. Wang, Q. Zhang, Z. Wang, Y. Liu, Y. Dai, B. Huang, X. Qin, X. Zhang, Synthesis of a WO$_3$ photocatalyst with high photocatalytic activity and stability using synergetic internal Fe^{3+} doping and superficial Pt loading for ethylene degradation under visible-light irradiation, Catal. Sci. Technol. 9 (2019) 652–658, https://doi.org/10.1039/C8CY02375A.

[44] H. Göksu, H. Burhan, S.D. Mustafov, F. Şen, Oxidation of benzyl alcohol compounds in the presence of carbonHybrid supported Platinum nanoparticles (Pt@CHs) in oxygen atmosphere, Sci. Rep. 10 (2020) 5439, https://doi.org/10.1038/s41598-020-62404-5.

[45] S. Saha, B. Martin, B. Leonard, D. Li, Probing synergetic effects between platinum nanoparticles deposited via atomic layer deposition and a molybdenum carbide nanotube support through surface characterization and device performance, J. Mate. Chem. A 4 (2016) 9253–9265, https://doi.org/10.1039/C6TA03198F.

[46] P. Sun, H. Liu, M. Feng, L. Guo, Z. Zhai, Y. Fang, X. Zhang, V.K. Sharma, Nitrogen-sulfur co-doped industrial graphene as an efficient peroxymonosulfate activator: singlet oxygen-dominated catalytic degradation of organic contaminants, Appl. Catal. B: Environ. 251 (2019) 335–345, https://doi.org/10.1016/j.apcatb.2019.03.085.

[47] C. Wang, J. Kim, V. Malgras, J. Na, J. Lin, J. You, M. Zhang, J. Li, Y. Yamauchi, Metal–organic frameworks and their derived materials: emerging catalysts for a sulfate radicals-based advanced oxidation process in water purification, Small 15 (2019) 1900744, https://doi.org/10.1002/smll.201900744.

[48] R. Niu, G. Wang, Y. Ding, S. Tang, X. Hu, J. Zhu, Hexagonal prism arrays constructed using ultrathin porous nanoflakes of carbon doped mixed-valence Co–Mn–Fe phosphides for ultrahigh areal capacitance and remarkable cycling stability, J. Mate. Chem. A 7 (2019) 4431–4437, https://doi.org/10.1039/C8TA11763B.

[49] R. Yin, R. Chen, S. He, W. Li, L. Zeng, W. Guo, M. Zhu, In situ photoreduction of structural Fe(III) in a metal–organic framework for peroxydisulfate activation and efficient removal of antibiotics in real wastewater, J. Hazard. Mater. 388 (2020) 121996, https://doi.org/10.1016/j.jhazmat.2019.121996.

[50] L. Chen, H. Ji, J. Qi, T. Huang, C.-C. Wang, W. Liu, Degradation of acetaminophen by activated peroxymonosulfate using Co(OH)$_2$ hollow microsphere supported titanate nanotubes: insights into sulfate radical production pathway through CoOH$^+$ activation, Chem. Eng. J. 406 (2021) 126877, https://doi.org/10.1016/j.cej.2020.126877.

[51] H. Ji, P. Du, D. Zhao, S. Li, F. Sun, E.C. Duin, W. Liu, 2D/1D graphitic carbon nitride/titanate nanotubes heterostructure for efficient photocatalysis of sulfamethazine under solar light: catalytic "hot spots" at the rutile–anatase–titanate interfaces, Appl. Catal. B: Environ. 263 (2020) 118357, https://doi.org/10.1016/j.apcatb.2019.118357.

[52] R. Xiao, Z. Luo, Z. Wei, S. Luo, R. Spinney, W. Yang, D.D. Dionysiou, Activation of peroxymonosulfate/persulfate by nanomaterials for sulfate radical-based advanced oxidation technologies, Curr. Opin. Chem. Eng. 19 (2018) 51–58, https://doi.org/10.1016/j.coche.2017.12.005.

[53] S. Luo, L. Gao, Z. Wei, R. Spinney, D.D. Dionysiou, W.-P. Hu, L. Chai, R. Xiao, Kinetic and mechanistic aspects of hydroxyl radical–mediated degradation of naproxen and reaction intermediates, Water Res. 137 (2018) 233–241, https://doi.org/10.1016/j.watres.2018.03.002.

[54] S. Wu, H. Liu, Y. Lin, C. Yang, W. Lou, J. Sun, C. Du, D. Zhang, L. Nie, K. Yin, Y. Zhong, Insights into mechanisms of UV/ferrate oxidation for degradation of phenolic pollutants: role of superoxide radicals, Chemosphere 244 (2020) 125490, https://doi.org/10.1016/j.chemosphere.2019.125490.

[55] K. Nord, J. Karlsen, H.H. Tønnesen, Photochemical stability of biologically active compounds. IV. Photochemical degradation of chloroquine, Int. J. Pharmaceut. 72 (1991) 11–18, https://doi.org/10.1016/0378-5173(91)90375-X.

[56] S. Doddaga, R. Peddakonda, Chloroquine-N-oxide, a major oxidative degradation product of chloroquine: Identification, synthesis and characterization, J. Pharm.

Biomed. Anal. 81-82 (2013) 118–125, https://doi.org/10.1016/j.jpba.2013.04.004.

[57] N. Bensalah, S. Midassi, M.I. Ahmad, A. Bedoui, Degradation of hydroxychloroquine by electrochemical advanced oxidation processes, Chem. Eng. J. 402 (2020) 126279, https://doi.org/10.1016/j.cej.2020.126279.